Elastic and inelastic scattering of 362 MeV polarized protons from ^{40}Ca

D. Frekers, S. S. M. Wong, R. E. Azuma, T. E. Drake, J. D. King,
L. Buchmann, and R. Schubank
Department of Physics, University of Toronto, Toronto, Canada M5S 1A7

R. Abegg, K. P. Jackson, C. A. Miller, and S. Yen
TRIUMF, Vancouver, Canada V6T 2A3

W. P. Alford and R. L. Helmer
Department of Physics, University of Western Ontario, London, Canada N6A 3K7

C. Broude
Department of Nuclear Physics, Weizmann Institute of Science, Rehovot, Israel

S. Mattsson
Department of Physics, Chalmers University, Göteborg, Sweden

E. Rost
Department of Physics, University of Colorado, Boulder, Colorado 80309
(Received 19 November 1986)

Scattering of 362 MeV polarized protons from ^{40}Ca to the ground, 3^- (3.74 MeV), 2^+ (3.90 MeV), and 5^- (4.49 MeV) states has been studied from 3° to 65° in the laboratory. Measured values of $d\sigma/d\Omega$ and A_y are compared with standard relativistic and nonrelativistic calculations using transition densities from random-phase-approximation calculations and electron scattering data.

I. INTRODUCTION

There is currently great interest in microscopic approaches to nucleon-nucleus scattering at intermediate energies due to the relative success in explaining experimental data and the connection of the nucleon-nucleon interaction with many-body theories.[1] Phenomenological optical potentials[2] are also very successful in reproducing both cross section and analyzing power data although they are often of limited significance because of the number of parameters involved.

In this paper, we present cross section and analyzing power measurements together with phenomenological and microscopic calculations for elastic and inelastic proton scattering to the low-lying states of ^{40}Ca. The measurements, which are the first ones made with the upgraded medium-resolution spectrometer (MRS) at TRIUMF, were carried out for an incident proton kinetic energy of 362 MeV and for scattering angles from 3° to 65°, which correspond to momentum transfers from 0.24 to 4.8 fm^{-1}. This is one of a series of papers[3] concerning the closed shell nuclei ^{40}Ca, ^{90}Zr, and ^{208}Pb, where, due to the large energy separation, low-lying levels can be isolated with an overall resolution of $\sim$100–120 keV on the MRS, and where electron scattering data are available to relatively large momentum transfer. For ^{40}Ca, measurements of the elastic and inelastic proton scattering cross section and analyzing power have been performed over a wide range of energies up to 1000 MeV as shown in Table I. Our measurements are taken to a much higher momentum transfer than most others.

For comparison of experimental data with available microscopic theories our incident proton energy is well chosen. Between 300 and 400 MeV, absorption is minimal and the effects of Pauli blocking and binding energy corrections, not included in microscopic relativistic impulse approximation calculations, are much less severe than at lower energies ($\lesssim$200 MeV).[4] From the nuclear structure point of view the closed-shell nucleus ^{40}Ca is well known, and shell model calculations fit electron scattering data.[5] The proton transition densities have been measured by inelastic electron scattering, and proton and neutron transition densities can be assumed identical for $N=Z$ nuclei.

The experiment will be presented in Sec. II. In Sec. III, we compare our elastic and inelastic data with conventional phenomenological model calculations while, in Sec. IV, we compare the data with microscopic Schrödinger and relativistic impulse approximation calculations using transition densities from random phase approximation calculations and from electron scattering data.

II. EXPERIMENT

The experiment was performed with the TRIUMF medium-resolution spectrometer (MRS).[6] A vertically dispersed beam of 362 MeV polarized protons was delivered onto a natural calcium target. The scattered beam was momentum analyzed in the vertical plane. A six quadrupole "twister," located upstream of the target,

was used to rotate the beam dispersion from the horizontal to the vertical plane to match the dispersion of the spectrometer. Target thickness was 25 mg/cm^2 for forward angles ($<18°$) and 50 mg/cm^2 for larger angles.

The MRS is a 1.5 GeV/c Q-D system with a design resolution of $dp/p = 10^{-4}$ and a momentum acceptance of 13%. The instrumentation consists of a low-pressure front-end wire chamber located at the target chamber exit and two drift chambers at the dipole exit, followed by an array of ten plastic scintillators to provide the reference time for the event trigger. Programmable emitter-couple-logic (ECL) -trigger electronics allow the user to define the momentum bite and time of flight acceptance through the spectrometer, and to insert additional trigger condi-

TABLE I. Summary of elastic and inelastic proton scattering measurements on ^{40}Ca.

Elastic				Inelastic			
E_p (MeV)	Angle range (deg)	q_{max} (fm^{-1})	Footnote	E_p (MeV)	Angle range (deg)	q_{max} (fm^{-1})	Footnote
<60	10—150	<2.3	a	<60	10—150	<2.3	a
61	30—105	2.7	b				
75	10—32	1.0	c				
80	5—95	2.9	d,e				
135	5—95	3.8	d				
153	5—70	3.2	c,f	150	25		g
155	6—35	1.7	h,i	155	5—55	2.6	f,h,i,j
156	5—54	2.6	k				
160	8—90	4.0	d,l				
175	6—40	2.0	m				
181	8—63	3.2	n				
182	4—38	2.0	o,p	182	10—43	2.2	o,p
185	4—42	2.2	q	185	4—42	2.2	q
300	4—38	2.6	r	334	2—9	0.7	s
362	3—65	4.8	present work	362	3—65	4.8	present work
400	3—35	2.9	r				
497	8—28	2.6	t				
500	3—30	2.8	r,u	500	5—30	2.8	u
613	3—31	3.4	v				
650	7—26	2.9	w	650	8—17	1.9	w
800	3—42	5.3	x,y	800	3—42	5.3	y,z
1000	6—18	2.7	aa	1000	3—18	2.7	aa

[a]R. Schaeffer, Nucl. Phys. A **132**, 186 (1969); C. R. Gruhn *et al.*, Phys. Rev. C **6**, 915 (1972).
[b]C. B. Fullmer *et al.*, Phys. Rev. **181**, 1565 (1969).
[c]C. Rolland *et al.*, Nucl. Phys. **80**, 625 (1966).
[d]A. Nadasen *et al.*, Phys. Rev. C **23**, 1023 (1981).
[e]P. Schwandt *et al.*, Phys. Rev. C **26**, 55 (1982).
[f]A. Willis *et al.*, Nucl. Phys. A **112**, 417 (1968); A. Willis *et al.*, J. Phys. **30**, 13 (1969).
[g]D. Newton *et al.*, Nucl. Phys. **67**, 449 (1965).
[h]R. Alphonce *et al.*, Nucl. Phys. **4**, 672 (1957).
[i]M. Liu *et al.*, Nucl. Phys. **75**, 481 (1966).
[j]R. M. Haybron *et al.*, Phys. Rev. **140B**, 638 (1965).
[k]V. Comparat *et al.*, Nucl. Phys. A **221**, 403 (1974).
[l]P. G. Roos *et al.*, Phys. Rev. **140B**, 1237 (1965).
[m]P. Hillman *et al.*, Nucl. Phys. **4**, 648 (1957).
[n]A. Johansson *et al.*, Ark. Fys. **19**, 541 (1961).
[o]H. Tyren and T. A. J. Maris, Nucl. Phys. **4**, 637 (1957).
[p]T. A. J. Maris and H. Tyren, Nucl. Phys. **4**, 662 (1957).
[q]J. Källne *et al.*, Phys. Scr. **2**, 195 (1970); A. Ingemarsson *et al.*, *ibid.* **2**, 191 (1970).
[r]D. Hutcheon (private communication).
[s]D. J. Horen *et al.*, Phys. Rev. C **30**, 709 (1984).
[t]G. W. Hoffmann *et al.*, Phys. Rev. Lett. **47**, 1436 (1981).
[u]K. K. Seth *et al.*, Phys. Lett. **158B**, 23 (1985).
[v]T. Bauer *et al.*, CEN Saclay Ann. Rep. 1977-78, p. 125.
[w]R. A. Miskimen *et al.*, Phys. Lett. **131B**, 26 (1983).
[x]L. Ray *et al.*, Phys. Rev. C **23**, 828 (1981).
[y]G. S. Adams *et al.*, Phys. Rev. C **21**, 2485 (1980).
[z]E. Bleszynski *et al.*, Phys. Rev. C **25**, 2563 (1982).
[aa]V. E. Starodubsky, Nucl. Phys. A **219**, 525 (1974).

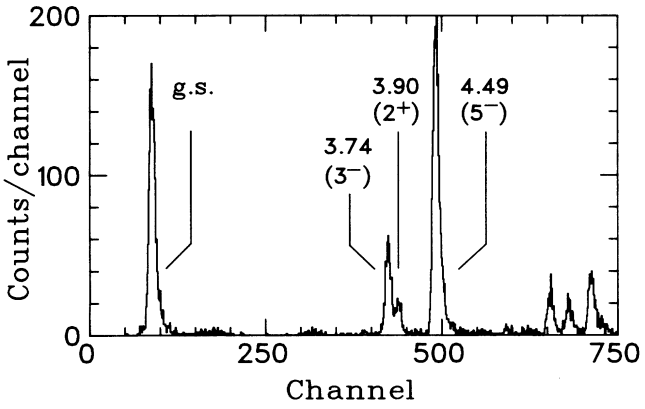

FIG. 1. Typical spectrum taken at 25° with the upgraded medium resolution spectrometer at TRIUMF for 362 MeV incident protons.

tions. For example, at extreme forward angles a thin scintillator, located near the focal plane, could be included in the trigger to allow prescaling of counts due to elastically scattered protons.

The front-end wire chamber provides a position resolution of better than 1 mm, corresponding to an angle resolution of better than 0.1°. Furthermore, it allows for a complete track reconstruction of the scattered particle, which eliminates sources not in the illuminated target area.

In the present ^{40}Ca($\vec{p}$,p′) experiment angular distributions from 3° to 65° in the laboratory frame were measured for elastic scattering and for transitions to excited states at 3.74 MeV (3_1^-), 3.90 MeV (2_1^+), and 4.49 MeV (5_1^-). MRS angle positions were determined from the kinematical overlap of protons inelastically scattered from the 4.44 or 7.65 MeV states in ^{12}C with protons elastically scattered from the hydrogen in a CH_2 target or, at large angles, by the overlap of protons inelastically scattered from the 3.74 and 4.49 MeV states in ^{40}Ca with protons elastically scattered from a small ^{16}O contaminant in the Ca target. Measured angles were found to agree within 0.1° with the spectrometer angle readout. The cross section was determined once the acceptance properties of the MRS were found by inserting a CH_2 target in place of the Ca target and comparing the measured cross section with the known values for elastic scattering from hydrogen.

An in-beam polarimeter, located upstream of the target, was used to monitor both the beam polarization and intensity. Downstream of the target, a secondary emission monitor also measured beam intensity and provided a check against the polarimeter measurement. Beam currents were typically in the subnanoampere region at very forward angles and up to 80 nA at large angles. Beam polarization was approximately 70% for either spin direction. To account for the deadtime of the system, pulser signals were injected at random times into the MRS trigger circuit. Detection efficiency of the system was determined to be between 90% and 95% and found to be only slightly dependent on the incident beam intensity. An overall energy resolution of $\sim$140 keV was achieved after applying various aberration corrections. A proton spectrum obtained at $\theta_{\rm lab}=25°$ is shown in Fig. 1. The 3^-, 2^+ doublet in ^{40}Ca at 3.74 and 3.90 MeV is clearly resolved. However, the cross section for the transition to the 2^+ state at larger angles is generally an order of magnitude smaller than that for the 3^- state. In this case the Landau tail from the 3^- peak makes the extraction of the 2^+ contribution difficult.

III. COMPARISON WITH PHENOMENOLOGICAL MODELS

A. Elastic scattering

The experimental data will be studied first by comparing with the calculated results of relativistic and nonrelativistic phenomenological optical models. In the nonrelativistic approach, the optical potential has the form

$$U(r)=V_{\rm Coul}(r)+U_0(r)-\left[\frac{\hbar}{m_\pi c}\right]^2\frac{1}{r}\frac{\partial}{\partial r}U_{\rm so}(r)\,\boldsymbol{\sigma}\cdot\mathbf{L}\ , \quad (1)$$

where the radial shape of each of the components of the complex potentials $U_0=V_0+iW_0$ and $U_{\rm so}=V_{\rm so}+iW_{\rm so}$ is given by a Woods-Saxon function

$$f(r,r_0,a)=\frac{1}{1+e^{(r-r_0A^{1/3})/a}}\ . \quad (2)$$

There are therefore twelve parameters (four strengths, V_0, W_0, $V_{\rm so}$, and $W_{\rm so}$ and the reduced radius r_0 and diffuseness a for each radial shape) to be determined by fitting to the data.[7] In Dirac phenomenology, the optical potential has the form

$$U(r)=U_{\rm scalar}(r)+\gamma^0[U_{\rm vector}(r)+V_{\rm Coul}(r)]\ , \quad (3)$$

where $U_{\rm scalar}(r)$ is a complex Lorentz scalar potential and $U_{\rm vector}(r)$ is a complex timelike component of a four-vector potential.[8] Again, the real and imaginary parts of the potentials are assumed to have Woods-Saxon shape, as given by Eq. (2), leaving also 12 parameters to be determined by experiment.

The optical potential search code RUNT (Ref. 7) was used to fit the elastic cross section and analyzing power data, and to determine the parameters for both the relativistic and the nonrelativistic approaches. The results are given in Fig. 2 with the full lines obtained from the relativistic calculation and the broken lines the nonrelativistic calculation. It is seen that both calculations give a good fit to the cross section. For the analyzing power the relativistic results are slightly better, except at the largest angles. The values of the optical potential parameters are given in Table II together with the volume integrals per nucleon, χ^2 values and total reaction cross sections σ_R. The best fit values obtained from our relativistic calculation follow the general trend of energy dependence of those given in Table I of Ref. 7. For the nonrelativistic calculations the parameters obtained are in general agreement with those found at 500 MeV by Seth *et al.*[9] and those used at 334 MeV by Horen *et al.*,[10] except that our radius parameter r_0 of the real potential is unphysically small. We will nevertheless use this set for inelastic calculations since a larger value for r_0 decreases the quality of the fit quite markedly. We note, however, that a small

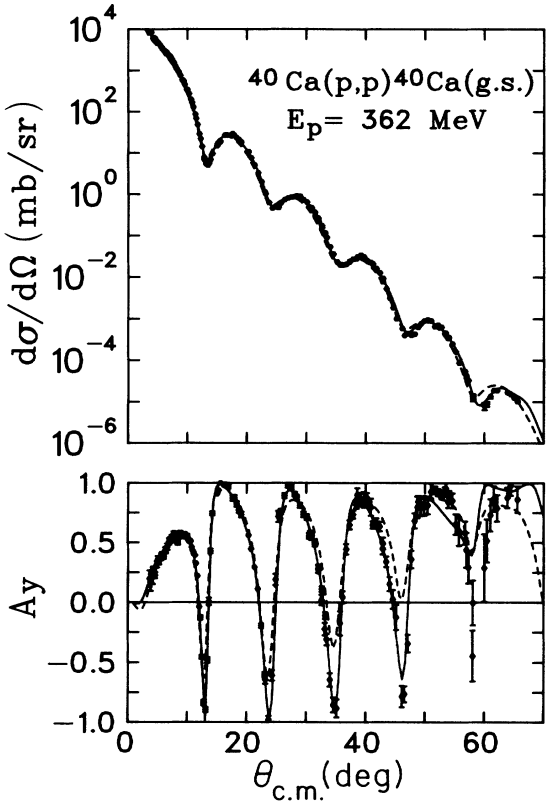

FIG. 2. Phenomenological optical model fit to elastic scattering at 362 MeV. The solid line is the result of a relativistic calculation and the dashed line the result of a nonrelativistic calculation.

TABLE II. Phenomenological optical potential parameters.

		Well depth (MeV)	Radius (fm)	Diffuseness (fm)	Volume integral per nucleon (MeV fm^3)
Relativistic phenomenological optical potential					
Vector	V	294.6	1.01	0.64	1690
	W	−97.0	1.12	0.55	−686
Scalar	V	−419.9	1.00	0.67	−2422
	W	99.0	1.12	0.54	698
$-R_R=0.6976$[a] $-R_I=-0.9839$[a] $\chi^2_\sigma/N_\sigma=16.7$[b] $\chi^2_P/N_P=4.46$[b] $\sigma_R=547$ mb[c]					
Nonrelativistic phenomenological optical potential					
	V	14.9	0.646	0.515	9.5
	W	−34.5	1.109	0.681	−332
	V_{so}	−3.86	1.006	0.703	−0.28
	W_{so}	4.342	0.997	0.703	0.85
$\chi^2_\sigma/N_\sigma=117$[b] $\chi^2_P/N_P=22$[b] $\sigma_R=530$ mb[c]					

[a] R_R (R_I) is the ratio of volume integrals of the real (imaginary) part of the vector and scalar potentials.
[b] $\chi^2_\sigma/N_\sigma(\chi^2_P/N_P)$ is the reduced χ^2 for the differential cross section (analyzing power).
[c] σ_R is the total reaction cross section.

value ($r_0=0.79$ fm) was also obtained by Seth *et al.* for the 500 MeV data.[9]

B. Inelastic scattering to low-lying natural parity states

Using the framework of the collective model, calculations for the cross section and analyzing power in inelastic scattering were carried out in the distorted wave Born approximation (DWBA). For the nonrelativistic calculation this was done in the usual fashion by deforming the real and imaginary parts of the central and spin-orbit potential determined earlier from elastic scattering. For the relativistic case the scalar, vector and Coulomb terms in the Dirac potential in Eq. (3) were deformed in the same way as the central potentials in the nonrelativistic case. From these, "Schrödinger-equivalent" potentials were obtained by reducing the Dirac equation to a Schrödinger-like equation for the upper component of the wave function.[11] The resulting deformed potentials, which can also be expressed in a form equivalent to that derived from Eq. (1) by deforming central and spin-orbit terms, can be put into a standard DWBA calculation. Thus, deformation parameters entering into these calculations are those for the scalar and vector potentials.

Differential cross sections and analyzing powers were

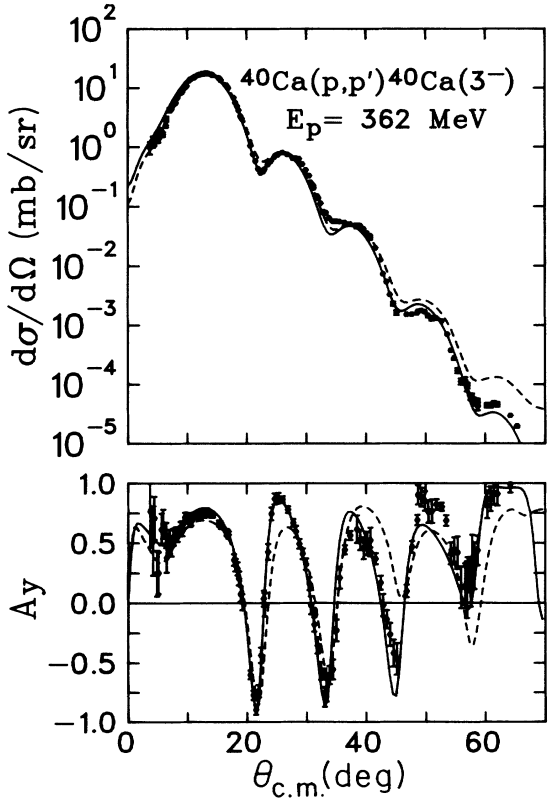

FIG. 3. Phenomenological collective model fit to inelastic scattering for the 3^- state at 3.74 MeV. The solid line is from a relativistic calculation and the dashed line is from a nonrelativistic calculation.

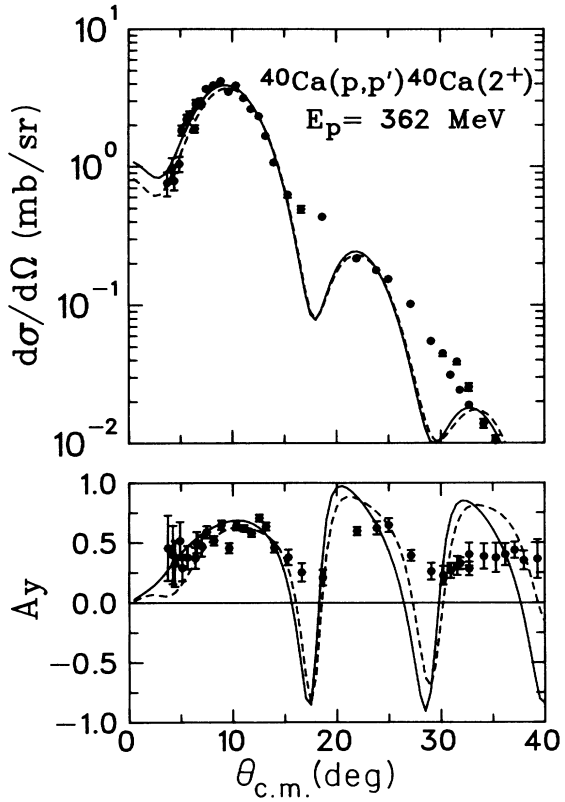

FIG. 4. Same as Fig. 3 except for the 2^+ state at 3.90 MeV.

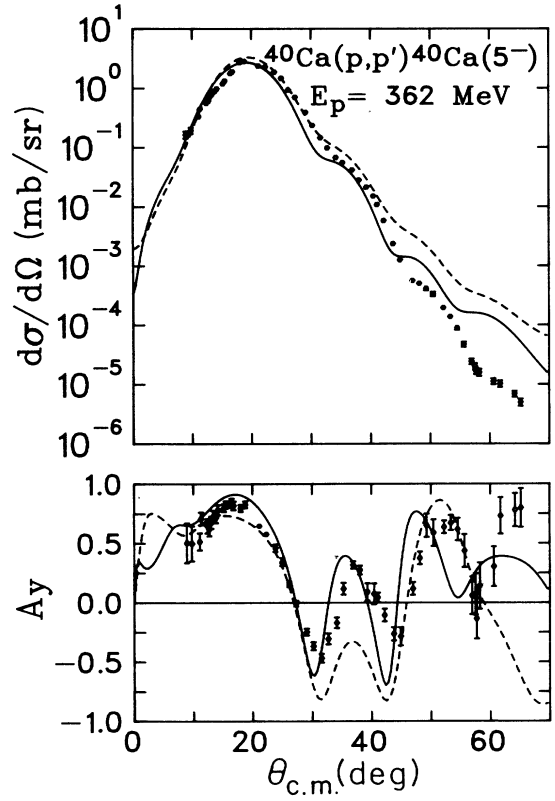

FIG. 5. Same as Fig. 3 except for the 5^- state at 4.49 MeV.

calculated for the 3^- (3.74 MeV), 2^+ (3.90 MeV), and 5^- (4.49 MeV) states of ^{40}Ca, using both approaches. The values of the deformation parameters β_λ for each state were adjusted to fit the data in such a way that the deformation length parameters $\delta_\lambda=\beta_\lambda R$ were kept the same for all components of the optical potential. Although the best-fit values for β_λ depend on the formalism and on the potential shapes used, the deformation length δ_λ is less sensitive to the details of the model used. As a result, we find no significant difference in the extracted values of δ_λ in spite of the large differences between the values of the radius parameters obtained for the relativistic and nonrelativistic optical potentials. Similar observations were also made in Ref. 11.

In Figs. 3—5 we show the measured cross section and analyzing power data for the 3^-, 2^+, and 5^- states in ^{40}Ca together with the results of the two calculations. The collective model description of the 3^- state is good over the whole angular range and a fairly good fit for the 5^- state is also obtained. On the other hand, the agreement with the experimental data is poor for the 2^+ state. This is to be expected in view of the lack of collectivity for the state as is evident from the small δ_2 value. The relativistic calculations produce an overall better agreement to the cross section data at large angles and to the analyzing power data over the whole angular range. The extracted deformation length parameters are $\delta_2=0.42$ fm, $\delta_3=1.22$ fm, and $\delta_5=0.69$ fm for both relativistic and nonrelativistic calculations.

Deformation length parameters δ_λ extracted from ^{40}Ca(p,p') reactions over a range from 25 to 1000 MeV are collected in Fig. 6 together with our values as well as those deduced from tabulated values[12] of $B(E\lambda)$ (dotted line). In the region of maximum nuclear transparency, around 200 MeV, the energy dependence of δ_3 seems to exhibit a shallow minimum. Such an energy dependence might arise from the difference in radial shape between the hadronic and electromagnetic transition operators,[13] but a recent study on inelastic excitation in ^{12}C, however,

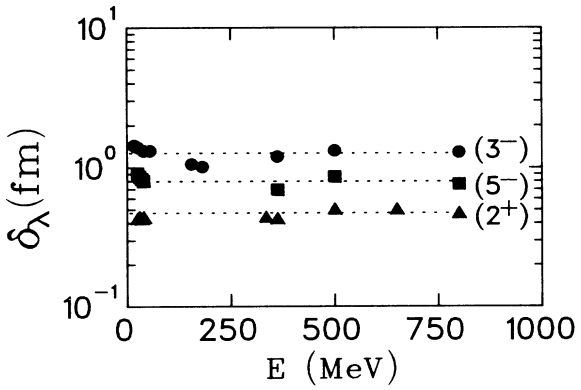

FIG. 6. Deformation length parameter as a function of the proton bombarding energy for the 3^- state at 3.74 MeV (circles), the 2^+ state at 3.90 MeV (triangles), and the 5^- state at 4.49 MeV (squares). The dashed lines represent the values deduced from transition probabilities $B(E\lambda)$. (Data taken from references in Table I.)

did not show any such effect.[14] It might also be due to the phenomenological fits to the data which do not uniquely determine the energy dependence of the imaginary parts of the optical potential.

IV. COMPARISON WITH MICROSCOPIC MODELS

The experimental data are compared in this section with the calculated results of both relativistic and nonrelativistic models in a microscopic approach. The primary purpose of the comparison is not to see whether the "Dirac" or "Schrödinger" method is superior in fitting the data; instead, we are interested in observing to what degree each model can account for the measured cross section and analyzing power using, as far as possible, the same set of input parameters derived directly from experimental data.

A. Elastic scattering

The starting point of this part of our analysis is the optical potential; we take here a "microscopic" approach by folding the ground state nucleon density with the nucleon-nucleon interaction, the same interaction used later for inelastic scattering. Since ^{40}Ca is a self-conjugate nucleus, we use as nucleon density the charge density derived from electron scattering.

A standard three-parameter Fermi form,

$$\rho_{\rm ch}=\rho_0\frac{1+w(r/R_0)^2}{1+e^{[(r-R_0)/a]}}\ , \tag{4}$$

is used for the charge density with the parameters,

$$R_0=3.766\ \text{fm},\quad a=0.586\ \text{fm},\quad w=-0.161\ , \tag{5}$$

taken from de Jager *et al.*;[15] ρ_0 is the normalization factor. Two different optical potentials, one in the relativistic impulse approximation,[16] and one with the density-dependent Hamburg nucleon-nucleon interaction in a nonrelativistic approach,[17] are then calculated with the same charge density as input. The results are shown in Fig. 7.

The nonrelativistic calculation (solid line) is in fair agreement with the data except for a shift in "phase" of the diffraction maxima and minima for both the differential cross section and the analyzing power and an overestimation of the magnitude of the first maximum in A_y. This might be due to the large momentum transfer range ($q \lesssim 4.8\ \text{fm}^{-1}$) of our data and the fact that the nucleon density was obtained from electron scattering data for momentum transfers $q \lesssim 3.2\ \text{fm}^{-1}$. We note that changes in the charge density radius and diffuseness parameters, for example to $R_0=3.35$ fm and $a=0.71$ fm, improve the fits to the data except for the first maximum in A_y. The results are given in Fig. 8 (solid lines).

For the relativistic calculation, the maxima and minima are also in fair agreement with the data but the differential cross section at most angles is too large and the oscillation in the analyzing power is not as pronounced as it is in the data (see dashed lines in Fig. 7). There are now two nucleon densities that enter, the scalar density $\rho_s(r)$ and the vector density $\rho_v(r)$; it is generally recommended to take $\rho_s(r)$ to be slightly smaller than $\rho_v(r)$ in order to account for the lower components of the Dirac wave functions.[16] Comparing with the experimental data, we found that the change in the results between $\rho_s(r)=0.95\rho_v(r)$ and $\rho_s(r)=\rho_v(r)$ is much less than the change arising from different input density parameters. From the nonrelativistic calculation described in the previous paragraph we have already concluded that, for our data, we need a nucleon density different from the charge density obtained from electron scattering measurements with a lower maximum momentum transfer. We therefore start with the density parameters, $R_0=3.35$ fm, $a=0.71$ fm, and $w=-0.161$, obtained earlier, to specify $\rho_v(r)$. For $\rho_s(r)$ we start from $a=0.71$ fm and $w=-0.161$, and make small adjustments to R_0 so as to get a better fit to our proton scattering data. The results are shown as dotted lines in Fig. 8. The best fit, however, was obtained for $R_0=3.56$ fm with $\rho_s(r)=\rho_v(r)$ and is shown as dashed lines in Fig. 8. The large improvement in describing the experimental data, especially at the minima and maxima of the diffraction patterns in the differential cross section and analyzing power, demonstrates again that a nucleon density different from the charge density given in Ref. 15 is required to describe the elastic scattering of protons

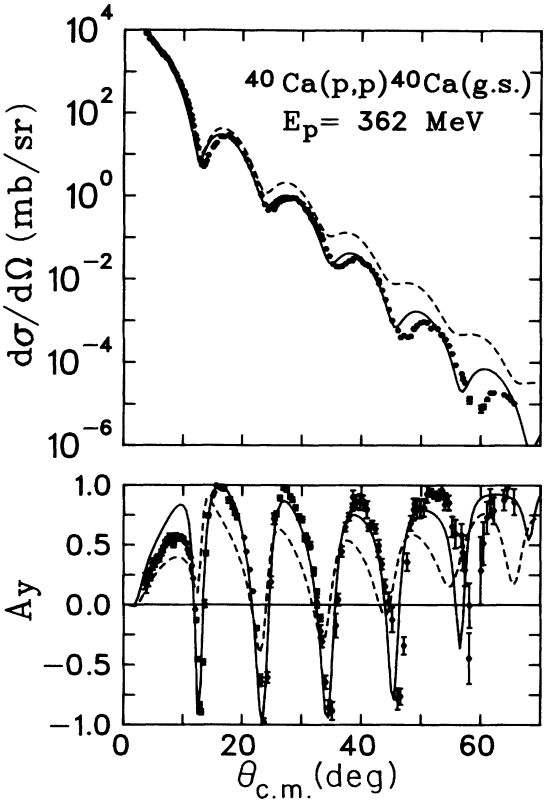

FIG. 7. Comparison of the elastic scattering data with microscopic relativistic (dashed lines) and nonrelativistic (solid lines) optical model calculations for the elastic scattering of 362 MeV protons from ^{40}Ca obtained using a three-parameter Fermi form with $R_0=3.766$ fm, $a=0.586$ fm, and $w=-0.161$ for the neutron and proton charge densities.

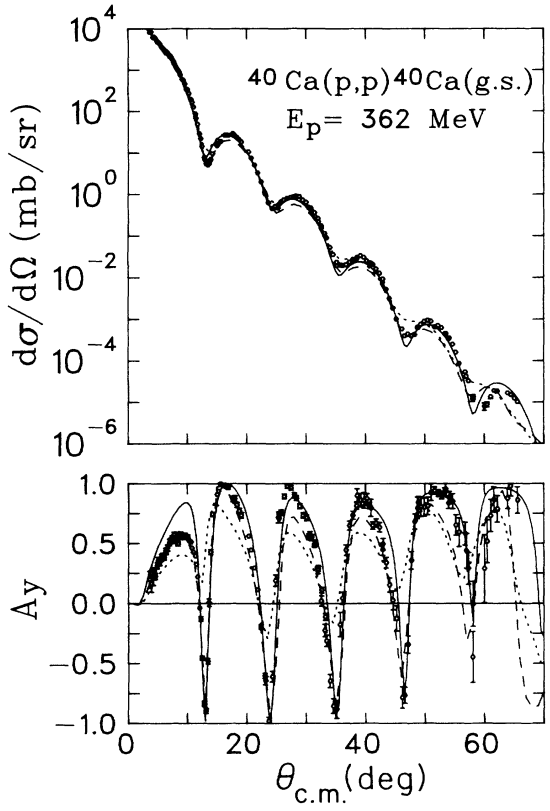

FIG. 8. Same as Fig. 7 except with $R_0=3.35$ fm, $a=0.71$ fm, and $w=-0.161$ for the nonrelativistic results (solid lines), and $R_0=3.56$ fm, $a=0.71$ fm, $w=-0.161$, and $\rho_s(r)=\rho_v(r)$ for the relativistic calculation (dashed lines). The dotted lines are the results of a relativistic calculation with $R_0=3.35$ fm, $a=0.71$ fm, and $w=-0.161$ for $\rho_v(r)$, and $R_0=3.76$ fm, $a=0.71$ fm, and $w=-0.161$ for $\rho_s(r)$.

from ^{40}Ca at 362 MeV. A good fit can also be obtained if a relativistic mean-field theory is used to generate the densities and a medium correction is applied to the interaction.[3] However, we did not pursue this line of study here since there is no simple nonrelativistic equivalent to such a calculation.

B. Inelastic scattering to low-lying natural parity states

The inelastic scattering data are compared with calculations both in the Dirac impulse approximation[18] (DRIA) and in the nonrelativistic distorted-wave Born approximation (DWBA),[1] using in each case the appropriate microscopic optical model potential obtained for elastic scattering. In addition to the optical potential and the nucleon-nucleus interaction, we also need a transition density to calculate the $(\vec{p},p')$ observables. For transitions to the 5^- and 3^- states, RPA densities are available. We used the Gillet force[5] to obtain a set of particle-hole amplitudes for each of the negative parity transitions via RPA and then transformed this set of amplitudes into the appropriate phase convention for each of the codes for calculating the differential cross section and analyzing power. Transition densities for the 5^-, 3^-, and 2^+ states in ^{40}Ca were also obtained from the inelastic electron scattering measurements of Seth *et al.*;[19] these are shown in Fig. 9 and compared with the RPA density for the 5^- state in Fig. 9(a) and for the 3^- state in Fig. 9(b).

The 5^- transition is the simplest one in RPA as there are only three independent particle-hole pairs which contribute to the transition density. The comparison with experimental data for electron scattering[20] is shown in Fig. 10 and with our $(\vec{p},p')$ data in Figs. 11 and 12. The nonrelativistic calculation gives a good description of the differential cross section but the analyzing power obtained with the Hamburg density-dependent force (solid line) is too low for $\theta_{c.m.}>30°$ although the diffraction pattern is correctly given. The results obtained with the two Love-Franey forces[21] show the same qualitative features when compared with the cross section data, but the analyzing power is much closer to the data at larger angles. In Fig. 11 only the results calculated with the more recent Love-Franey force are shown (dotted line). No significant difference in the calculated results for inelastic scattering is found when different optical model potentials, given earlier for elastic scattering, are used; the results shown are those calculated with the nucleon density parameters given by Eq. (5).

For the 5^- transition, the contribution of each particle-hole amplitude to the transition density can in principle be found by fitting to the electron scattering data. However, the electron scattering transition densities are usually described by a limited number (seven in this case) of Fourier-Bessel coefficients, and in a given shell-model space the degrees of freedom are given by the amplitude and phase of each particle-hole pair as well as by the parameter(s) required to describe the radial part of the single-particle wave function (e.g., the oscillation parameter if an harmonic-oscillator radial shape is used). Furthermore, particle-hole pairs with the same radial quantum numbers cannot be distinguished through the shape of electron scattering form factors. For harmonic-oscillator single-particle radial wave functions, a distinction between some of the particle-hole pairs, for example,

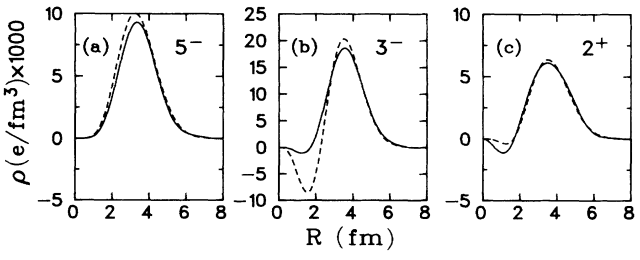

FIG. 9. Comparison of electron scattering transition densities for (a) the 5^- state at 4.49 MeV and (b) the 3^- state at 3.74 MeV given by Fourier-Bessel coefficients extracted from experimental data (solid lines) and calculations using RPA (dashed lines), and for (c) the 2^+ state at 3.90 MeV given by Fourier-Bessel coefficients (solid line) and best-fit single-particle transition density (dashed line).

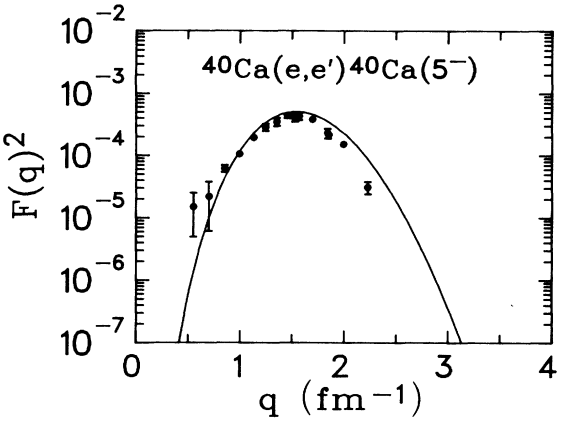

FIG. 10. Comparison of the form factor calculated with the RPA transition density with the electron scattering data of Itoh *et al.* (Ref. 20), for the 5^- state at 4.49 MeV.

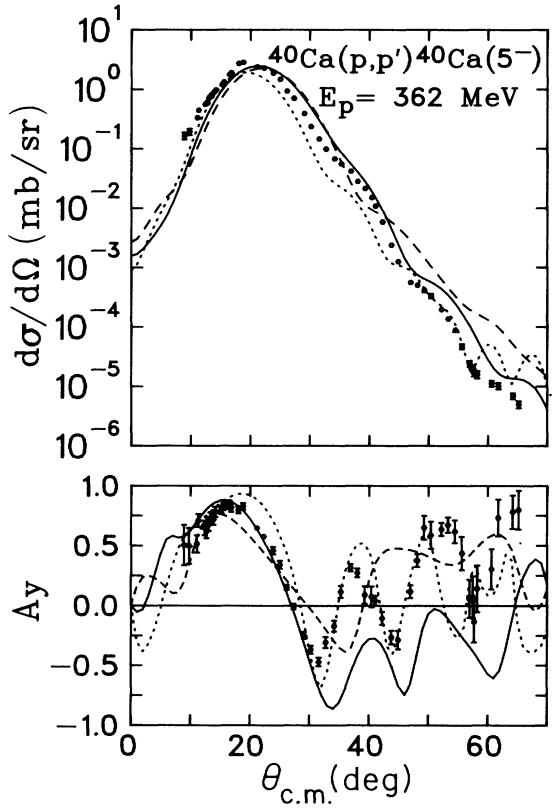

FIG. 11. Comparison of inelastic scattering data with non-relativistic distorted wave calculations for differential cross section and analyzing power for the ^{40}Ca($\vec{p}$,p') reaction at 362 MeV leading to the 5^- state at 4.49 MeV: (a) solid lines for microscopic optical potential with Hamburg density-dependent force and RPA transition density; (b) dashed lines, same as (a) except with transition density fitted to electron scattering data; and (c) dotted lines, same as (a) except with 1985 Love-Franey force.

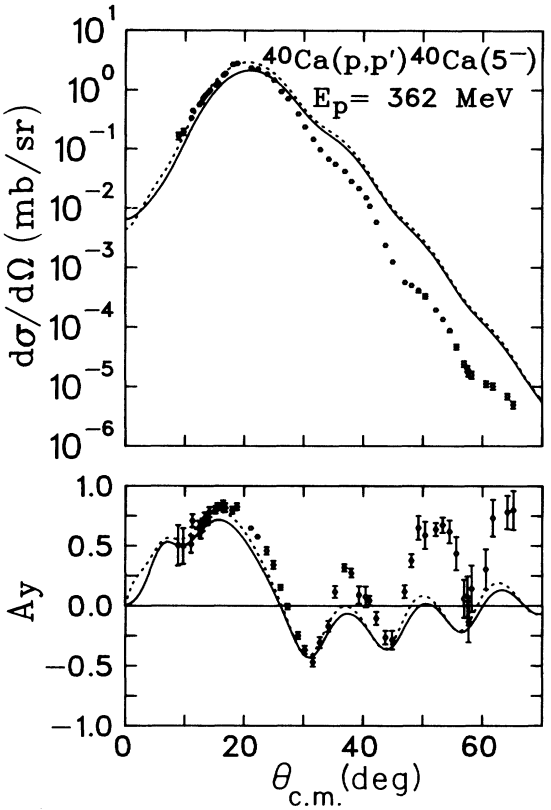

FIG. 12. Comparison of inelastic scattering data with relativistic distorted wave calculations for differential cross section and analyzing power for the ^{40}Ca($\vec{p}$,p') reaction at 362 MeV leading to the 5^- state at 4.49 MeV: (a) solid lines for RPA transition density; (b) dotted lines for transition density fitted to electron scattering result.

$1f_{7/2}1d_{5/2}^{-1}$ and $1f_{5/2}1d_{3/2}^{-1}$, can be made only by assuming different oscillator parameters for single-particle states of different j and the same n and l, but there is a very limited amount of this type of maneuvering that can be carried out meaningfully. (The situation is not basically different if more realistic single-particle wave functions are used.) Our calculations with the density-dependent force and with a transition density fitted to electron scattering show an analyzing power at large angles in better overall agreement with the data (dashed line in Fig. 11). A relativistic calculation using a transition density fitted to electron scattering (dotted line in Fig. 12) does not give a significantly different fit to the data.

The results of the relativistic calculations are not too different from those of the non-relativistic calculations as far as the overall trend is concerned. They are in very close agreement with the data for angles smaller than 30°. The most notable difference from experiment is that the differential cross section is too high at $\theta > 30°$. The analyzing power fit, on the other hand, is slightly better here although the maxima and minima of the diffraction pattern are still much smaller (in absolute value) than the data. Again, different optical model potentials as given by variations of the input nucleon density parameters do

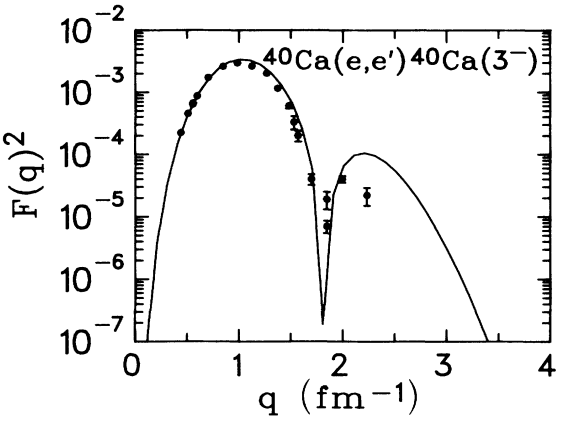

FIG. 13. Comparison of the form factor calculated with the RPA transition density with the electron scattering data of Itoh *et al.* (Ref. 20) for the 3^- state at 3.74 MeV.

not give any significant changes; the $\rho_s(r)=\rho_v(r)$ set given above is used for the solid line fit shown in Fig. 12.

From the nuclear structure point of view, the excitation of the 3^- state is far more complicated. In the $1\hbar\omega$ space, it involves nine distinct particle-hole pairs and the RPA amplitudes reproduce the electromagnetic charge form factor quite well (Fig. 13) and give a good description of our experimental data. The non-relativistic calculations, both with the density-dependent force (solid line in Fig. 14) and with the Love-Franey force (dotted line in Fig. 14), follow the data. The relativistic calculation (Fig. 15) shows the same general behavior as noted for the 5^- state—cross section too big at large angles and maxima and minima in the analyzing power not so pronounced. However, as far as the analyzing power is concerned, the overall agreement with the data is roughly the same as for the nonrelativistic calculations. Because of the large number of particle-hole pairs involved in the 3^- excitation, it is not possible to obtain a unique microscopic transition density from the electron scattering data, and no calculation with the transition density constrained by (e,e') results was done. A high degree of collectivity can be built up in the large 3^- space, and we observe that, for this transition, the RPA calculations reproduce reasonably well both the charge form factor from electron scattering

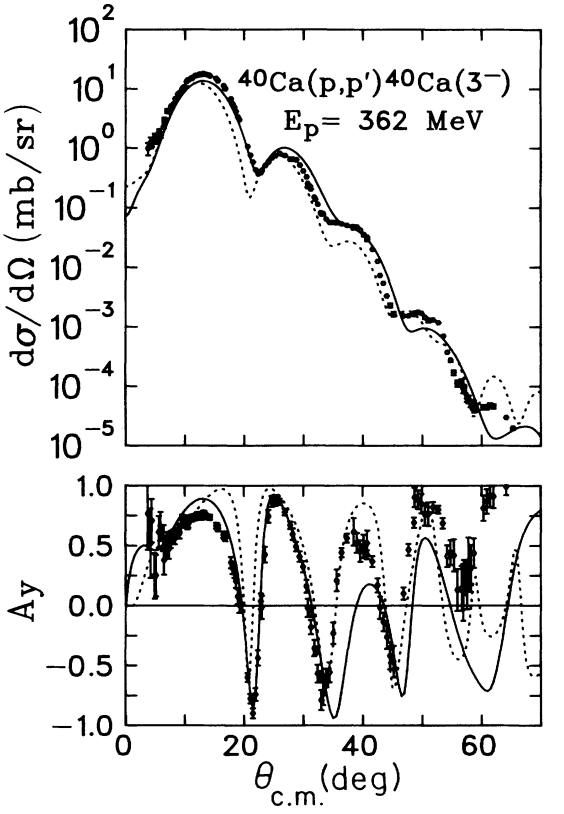

FIG. 14. Comparison of inelastic scattering data with non-relativistic distorted wave calculations for differential cross section and analyzing power for the $^{40}Ca(\vec{p},p')$ reaction at 362 MeV leading to the 3^- state at 3.74 MeV: (a) solid lines for microscopic optical potential, Hamburg density-dependent force and RPA transition density; (b) dotted lines, same as (a) except with 1985 Love-Franey force.

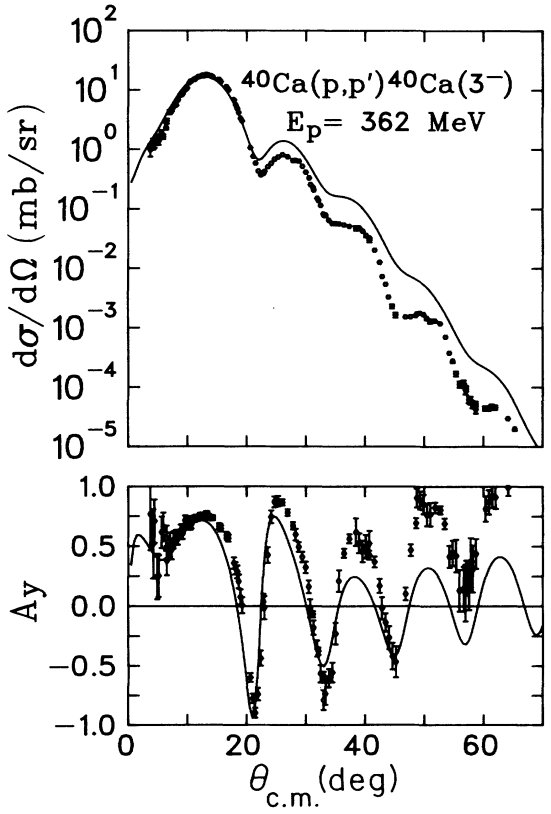

FIG. 15. Comparison of inelastic scattering data with a relativistic distorted wave calculation for differential cross section and analyzing power for the $^{40}Ca(\vec{p},p')$ reaction at 362 MeV leading to the 3^- state at 3.74 MeV obtained with RPA transition density.

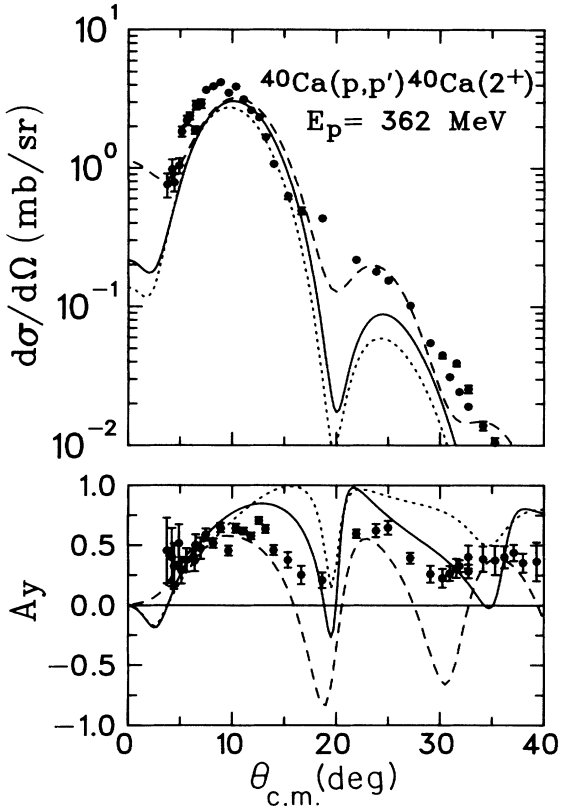

FIG. 16. Comparison of inelastic scattering data with calculations using microscopic models for differential cross section and analyzing power for the ^{40}Ca($\vec{p}$,p') reaction at 362 MeV leading to the 2^+ state at 3.90 MeV: (a) solid lines for nonrelativistic, microscopic optical potential, Hamburg density-dependent force and best-fit single particle transition density; (b) dotted lines, same as (a) except with 1985 Love-Franey force; (c) dashed lines, relativistic calculation with the same transition density.

and the cross section and analyzing power from our ($\vec{p}$,p') data.

For the 2^+ transition density, a proper microscopic nuclear structure calculation cannot be carried out easily since the shell model space required is very large, involving at least $2\hbar\omega$ excitations. We therefore start with the electron scattering results and obtain a set of particle-hole amplitudes by fitting to a minimum set of one-particle—one-hole excitations in the space of $1d_{3/2}$, $1f_{7/2}$, and $2p_{3/2}$ orbitals only. The results of this fitting are given in Fig. 16 for comparison with the data.

V. DISCUSSION

In the two previous sections we have considered our present results for elastic and inelastic scattering of 362 MeV protons from ^{40}Ca first from a phenomenological and second from a microscopic approach. In each case both a relativistic and a nonrelativistic formulation was used. Substantial success has been achieved with all models in describing the cross section and analyzing power at low momentum transfer for the elastic and inelastic transitions considered. Although more sophisticated analyses, both relativistic and nonrelativistic, can be carried out with our data, we choose not to do them here. It has been established that these better models will improve somewhat the fit to the data in particular those at the larger momentum transfer we are interested in here. However, until more experimental information becomes available for different targets and different bombarding energies, we cannot learn anything new about the reaction process beyond reconfirming what is already known.

A guiding principle in our microscopic analyses was to start, as far as possible, with parameters determined by independent experiments. In the case of elastic scattering, we found that the charge density determined by electron scattering could not be used to obtain an optical model potential that would fit our proton elastic scattering data in either a relativistic or a nonrelativistic calculation. This result may seem to be surprising in view of the excellent fit at 497 MeV.[16] However, the maximum momentum transfer reached in the present experiment is almost a factor of 2 larger even though the difference in the bombarding energy is only 145 MeV.

A slightly modified set of charge-density parameters, on the other hand, was able to fit the data up to $\sim$4.8 fm^{-1}. If the reason for the discrepancy is due to the higher maximum momentum transfer involved in our data, it would be interesting to see if electron scattering to higher momentum transfer would result in a set of charge density parameters similar to the ones we have found in fitting the proton scattering data. Of course, one may also question whether the simple approach of folding the charge density to obtain an optical potential is valid to high momentum transfer. For the relativistic calculation, we have further the problem that the input NN t matrix may not be adequate for nucleon-nucleus scattering $\gtrsim 30°$.

The inelastic scattering data are more sensitive to the nucleon-nucleus interaction. In addition to the optical potential, which depends on the nucleon-nucleus interaction weighted by the nucleon density, the (inelastic) transition in the target nucleus depends directly on the interaction with the incident proton. In fact the sensitivity is often used as a *filter* to examine the different parts of the interaction by selecting specific transitions. On the other hand the result depends also on the transition density from the ground to the excited state in question. We have used both electron scattering data and RPA calculations to obtain transition densities but this adds further uncertainty to the analysis.

All model calculations give reasonable agreement at small angles ($\lesssim 30°$). As momentum transfer increases, differences between the calculations and the data, and between calculations themselves, become more apparent. In spite of producing a marked improvement in the elastic scattering fit, the changes in the optical model potential are not able to significantly alter the difference between the measured and calculated results for inelastic scattering. It is possible that the one major shell excitation model space we have used for the 3^- and 5^- transitions is too small for the momentum transfer involved.

Although a large amount of analysis has been applied here to our data, it is by no means exhaustive. In both relativistic and nonrelativistic approaches, calculations can be done that will give results in better agreement with our experimental results. Our basic conclusion is that although intermediate energy proton-nucleus scattering is well described by both relativistic and nonrelativistic calculation for small momentum transfer, discrepancies occur as momentum transfer increases. On the other hand, we would like to refrain from drawing any further conclusion until a global analysis of a large set of data involving various targets, a wide range of energies, and large momentum transfer is carried out. The input to the calculations (the nucleon-nucleon interaction, the nucleon density of the target nucleus and the transition density) must also cover the same range of momentum transfer so as to maintain self-consistency in the different paths of the calculation.

ACKNOWLEDGMENTS

The authors wish to acknowledge the valuable contributions of Ali Zaringhalem. This work was supported in part by the Natural Sciences and Engineering Research Council of Canada.

[1]L. Rikus and H. V. von Geramb, Nucl. Phys. **A426**, 496 (1984).
[2]P. Schwandt, *in Proceedings of the Conference on the Interaction Between Medium Energy Nucleons in Nuclei—1982,* AIP Conf. Proc. No. 97, edited by H. O. Meyer (AIP, New York, 1983), p. 89.
[3]C. A. Miller *et al.*, Phys. Lett. **169B**, 166 (1986).
[4]C. Horowitz and D. Murdock, Phys. Lett. **168B**, 31 (1986).
[5]V. Gillet and E. A. Sanderson, Nucl. Phys. **A91**, 292 (1967).
[6]A. Miller, in University of Alberta/TRIUMF Workshop on Studying Nuclei with Medium Energy Protons, TRIUMF Report TRI-83-3, 1983, p. 399.
[7]A. M. Kobos, E. D. Cooper, J. I. Johansson, and H. S. Sherif, Nucl. Phys. A **445**, 605 (1985). The optical model code RUNT was developed by E. D. Cooper, Ph.D. thesis, University of Alberta, 1981 (unpublished).
[8]B. C. Clark, S. Hanna, and R. L. Mercer, in Ref. 2, p. 260.
[9]K. K. Seth *et al.*, Phys. Lett. **158B**, 23 (1985).
[10]D. J. Horen *et al.*, Phys. Rev. C **30**, 709 (1984).
[11]H. S. Sherif, R. I. Sawafta, and E. D. Cooper, Nucl. Phys. **A449**, 709 (1986).
[12]P. M. Endt and C. van der Leun, Nucl. Phys. **A310**, 1 (1978).
[13]F. Osterfeld, J. Wambach, H. Lenske, and J. Speth, Nucl. Phys. **A318**, 45 (1979).
[14]K. W. Jones *et al.*, Phys. Rev. C **33**, 17 (1986).
[15]C. W. de Jager, H. de Vries, and C. de Vries, At. Data Nucl. Data Tables **14**, 479 (1974).
[16]J. A. McNeil, J. R. Shepard, and S. J. Wallace, Phys. Rev. Lett. **50**, 1439 (1983); J. R. Shepard, J. A. McNeil, and S. J. Wallace, *ibid.* **50**, 1443 (1983).
[17]H. von Geramb and K. Nakano, in Ref. 2, p. 44.
[18]E. Rost, J. R. Shepard, E. R. Siciliano, and J. A. McNeil, Phys. Rev. C **29**, 209 (1984). J. R. Shepard, E. Rost, and J. Piekarewicz, *ibid.* **30**, 1604 (1984).
[19]K. K. Seth *et al.* (private communiation).
[20]K. Itoh, M. Oyamada, and T. Torizuka, Phys. Rev. C **2**, 2181 (1970).
[21]W. G. Love and M. A. Franey, Phys. Rev. C **24**, 1073 (1981); **31**, 488 (1985).